

## Symmetry and lattice mismatch induced strain accommodation near and away from correlated perovskite interfaces

A. Vailionis, H. Boschker, Z. Liao, J. R. A. Smit, G. Rijnders, M. Huijben, and G. Koster

Citation: *Applied Physics Letters* **105**, 131906 (2014); doi: 10.1063/1.4896969

View online: <http://dx.doi.org/10.1063/1.4896969>

View Table of Contents: <http://scitation.aip.org/content/aip/journal/apl/105/13?ver=pdfcov>

Published by the [AIP Publishing](#)

---

### Articles you may be interested in

[Effect of lattice-misfit strain on the process-induced imprint behavior in epitaxial Pb \( Zr 0.52 Ti 0.48 \) O 3 thin films](#)

*Appl. Phys. Lett.* **85**, 1583 (2004); 10.1063/1.1786662

[Magnetic domain structure and lattice distortions in manganite films under tensile strain](#)

*J. Appl. Phys.* **93**, 8322 (2003); 10.1063/1.1558716

[Perovskite oxide tricolor superlattices with artificially broken inversion symmetry by interface effects](#)

*Appl. Phys. Lett.* **81**, 4793 (2002); 10.1063/1.1530734

[Microstructure and magnetic properties of strained La 0.7 Sr 0.3 MnO 3 thin films](#)

*J. Appl. Phys.* **88**, 4257 (2000); 10.1063/1.1309040

[Epitaxial strain induced metal insulator transition in La 0.9 Sr 0.1 MnO 3 and La 0.88 Sr 0.1 MnO 3 thin films](#)

*Appl. Phys. Lett.* **76**, 155 (2000); 10.1063/1.125687

---

An advertisement for COMSOL Multiphysics. On the left, there is a 3D rendering of a mechanical part with a red and yellow color gradient, likely representing temperature or stress distribution. To the right, the text "Over 600 Multiphysics Simulation Projects" is displayed in large, white, sans-serif font. Below this text is a blue button with the text "VIEW NOW >". In the bottom right corner, the COMSOL logo is shown, consisting of a stylized "C" icon followed by the word "COMSOL".

# Symmetry and lattice mismatch induced strain accommodation near and away from correlated perovskite interfaces

A. Vailionis,<sup>1</sup> H. Boschker,<sup>2,3</sup> Z. Liao,<sup>2</sup> J. R. A. Smit,<sup>2</sup> G. Rijnders,<sup>2</sup> M. Huijben,<sup>2</sup> and G. Koster<sup>2</sup>

<sup>1</sup>Geballe Laboratory for Advanced Materials, Stanford University, Stanford, California 94305, USA

<sup>2</sup>MESA+ Institute for Nanotechnology, University of Twente, 7500 AE Enschede, The Netherlands

<sup>3</sup>Max Planck Institute for Solid State Research, 70569 Stuttgart, Germany

(Received 23 July 2014; accepted 19 September 2014; published online 30 September 2014)

Distinct  $\text{MnO}_6$  octahedral distortions near and away from the  $\text{La}_{0.67}\text{Sr}_{0.33}\text{MnO}_3/\text{SrTiO}_3(001)$  (LSMO/STO) interface are quantified using synchrotron x-ray diffraction and dynamical x-ray diffraction simulations. Three structural regions of stress accommodation throughout the film thickness were resolved: near the LSMO/STO interface, intermediate region farther from the interface, and the main layer away from the interface. The results show that within the first two unit cells stress is accommodated by the suppression of octahedral rotations in the film, leading to the expansion of the  $c$ -axis lattice parameter. Farther from the interface film structure acquires octahedral tilts similar to thicker perovskite films under tensile stress, leading to a reduced  $c$ -axis parameter. We demonstrate that these regions are related to two different strain coupling mechanisms: symmetry mismatch at the interface and lattice mismatch in the rest of the film. The findings suggest new routes for strain engineering in correlated perovskite heterostructures. © 2014 AIP Publishing LLC.

[<http://dx.doi.org/10.1063/1.4896969>]

Transition-metal oxides with  $\text{ABO}_3$  perovskite-type structure exhibit strong electron-lattice correlations which govern physical properties in these materials, such as colossal magnetoresistance, ferroelectricity, superconductivity, and charge ordering. For example, in manganites, the desired transport and magnetic properties are greatly influenced by complex interplay between charge, spin, lattice, and orbital degrees of freedom and therefore exhibit a very rich phase diagram, which is affected by ionic radii, stress/strain/pressure, anion and cation stoichiometry, and substitutional doping.<sup>1</sup> In epitaxial thin films, some functional properties can be effectively controlled by a substrate induced in-plane biaxial stress. As the unit cell of the film attempts to accommodate the in-plane lattice parameter of the underlying single crystal substrate, the  $\text{ABO}_3$  perovskite structural unit deforms causing distortions of the  $\text{BO}_6$  octahedra. Until recently, mainly the  $\text{BO}_6$  octahedral deformations (change in size and shape) were used to understand mismatch strain accommodation in perovskite oxide heterostructures.<sup>2</sup> This approach led to prediction and synthesis of a ferroelectric ferromagnet  $\text{EuTiO}_3$  by using single parameter—biaxial strain.<sup>3,4</sup> The Jahn-Teller (J-T) type octahedral deformations were used to explain a reduction of ferromagnetic  $T_C$  as a function of biaxial stress in “colossal” magnetoresistance (CMR) manganites by Millis *et al.* employing general elasticity theory.<sup>5</sup> Here, the stress is accommodated by straining Mn-O bonds in a pseudocubic perovskite unit cell which induces deformation of the  $\text{MnO}_6$  octahedra, causing J-T based electron-phonon coupling. However, the assumed elastic deformations of  $\text{MnO}_6$  octahedra cannot explain the structural properties of epitaxial and coherent  $\text{La}_{1-x}\text{Sr}_x\text{MnO}_3$  thin films that are 2–8 unit cells thick. Mainly, the  $\text{La}_{0.7}\text{Sr}_{0.3}\text{MnO}_3$  ultrathin films grown coherently on  $\text{SrTiO}_3(001)$  (STO) are under tensile stress but exhibit elongated out-of-plane lattice parameter which is at

odds with the expected contraction.<sup>6</sup> The indirect evidence of such elongated  $c$ -axis lattice parameter in ultrathin LSMO/STO(001) films was also suggested by Tebano *et al.* and Lee *et al.* using x-ray magnetic circular dichroism (XMCD) where they observed a preferential occupation of  $(3z^2 - r^2)$  orbitals implying J-T type of distortions at the film-substrate interface.<sup>7,8</sup>

In this letter, we show that the interfacial out-of-plane lattice parameter expansion can be explained by including two effects: deformations and tilts/rotations of the  $\text{BO}_6$  octahedra. In thicker perovskite thin film heterostructures, the pattern and the degree of  $\text{BO}_6$  octahedra rotations can be modified by changing the sign and the magnitude of a mismatch strain.<sup>9,10</sup> Such strain-induced octahedral rotations directly affect magnetic and transport properties in thin epitaxial  $\text{SrRuO}_3$  (SRO) and  $\text{La}_{0.67}\text{Sr}_{0.33}\text{MnO}_3$  (LSMO) films.<sup>11,12</sup> At the film-substrate interface, the octahedral rotational pattern can be modified by the crystallographic symmetry mismatch of film and substrate unit cells.<sup>13–18</sup> The octahedral rotations induced by the symmetry mismatch across the film-substrate interface usually leads to Jahn-Teller type octahedral deformations. For example, in ultrathin LSMO films grown on (110)-oriented STO substrates, the octahedral coupling across the interface induces distinctive  $\text{BO}_6$  octahedra distortions leading to a high-temperature magnetic insulating phase, which makes the LSMO/STO(110) perovskite heterostructure a possible candidate for an insulating tunneling barrier in room temperature spin polarized tunneling devices.<sup>19</sup> From the application point of view, it is therefore essential to understand the origin of structural modifications at the interfaces of correlated oxide heterostructures.

Here, using synchrotron x-ray diffraction (XRD) and dynamical x-ray diffraction simulations, we reveal a rather complex stress accommodation mechanism in coherent

$\text{La}_{0.67}\text{Sr}_{0.33}\text{MnO}_3$  films grown on STO(001) substrate under tensile stress. Three structurally different regions were resolved: (i) two unit cell (u.c.) thick layer at the LSMO/STO interface with elongated out-of-plane lattice parameter, (ii) intermediate layer whose thickness varies with total film thickness, and (iii) rest of the layer away from the interface. At the interface,  $\text{MnO}_6$  octahedral rotations are suppressed causing elongation of the (001)-oriented Mn-O bond. Farther from the interface, the rotations acquire a pattern that is observed in thicker LSMO thin films under tensile stress with suppressed *c*-axis lattice parameter.<sup>10</sup> Here, the rotational pattern is imposed by the lattice mismatch between film and substrate and is caused by a coupling between octahedral rotations and biaxial strain, i.e., strain is accommodated by changing the film's unit cell size via rotations of corner-connected  $\text{MnO}_6$  units. We show that the lack of rotations at the LSMO/STO interface and subsequent unusual *c*-axis lattice expansion is not caused by conventional lattice mismatch but is rather induced by crystallographic symmetry mismatch between LSMO and STO structures across the interface. The observed LSMO structure at the interface might affect magnetic and transport properties and therefore contribute to the “dead layer” phenomena even in nearly perfect perovskite oxide heterostructures. These findings provide practical ways in searching for alternate substrate materials or buffer layers with similar crystallographic rotational patterns as that of LSMO.

Thin LSMO films used in this study were grown by pulsed-laser deposition (PLD) from a stoichiometric  $\text{La}_{0.67}\text{Sr}_{0.33}\text{MnO}_3$  target on  $\text{TiO}_2$ -terminated  $\text{SrTiO}_3(100)$  substrates by applying a KrF excimer laser at a repetition rate of 1 Hz and a laser fluence of  $2 \text{ J/cm}^2$ .<sup>20</sup> During growth, the substrate was held at  $750^\circ\text{C}$  in an oxygen environment in the range of 100–300 mTorr. The growth was monitored *in situ* by reflective high energy electron diffraction (RHEED) analysis allowing precise control of the thickness at the unit cell scale and accurate characterization of the growth dynamics.<sup>21</sup> For these conditions, a growth rate of  $\sim 0.16 \text{ \AA/s}$  was determined. After the growth, samples were slowly cooled to room temperature in 1 atm of oxygen at a rate of  $\sim 5^\circ\text{C/min}$  to optimize the oxidation level. The low level of surface roughness was confirmed by atomic force microscopy analysis (not shown), indicating smooth terraces separated by clear, single unit cell height steps similar to the surface of the initial  $\text{TiO}_2$ -terminated STO(001) substrate. X-ray diffraction measurements were performed at the Stanford Synchrotron Radiation Lightsource, beam line 7–2 and at the Stanford Nano Shared Facilities. X-ray diffraction calculations were carried out using GID\_sl program for simulating dynamical x-ray diffraction from strained crystals, multilayers, and superlattices, developed by Stepanov.<sup>22</sup>

Four LSMO(001) films with thicknesses of 10, 20, 40, and 60 nm were used in this study. The magnetic properties were determined by vibrating sample magnetometry (VSM) measurements in a Quantum Design PPMS system. The LSMO films exhibited optimal magnetic behavior, e.g., the 60 u.c. thick LSMO film displayed a Curie temperature of 350 K, in good agreement with the previous reports.<sup>23,24</sup> The measured and fitted x-ray diffraction patterns around the LSMO/STO(002) Bragg reflection for 10 and 60 nm thick

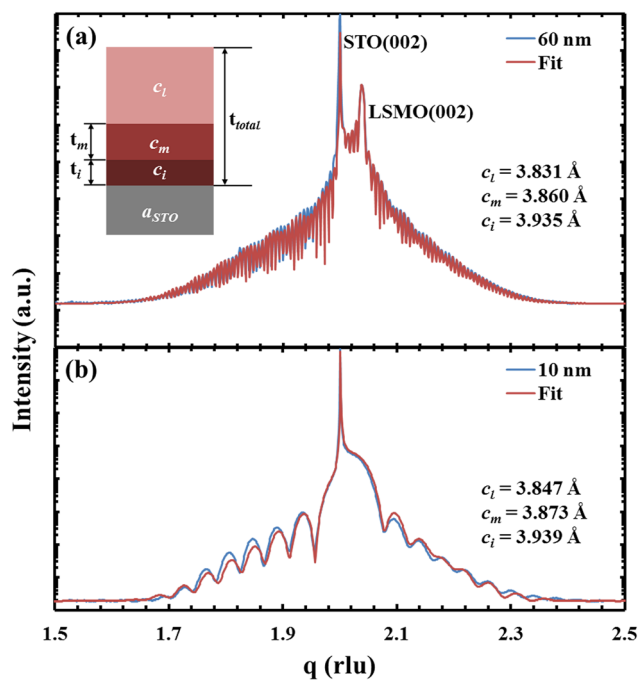


FIG. 1. Experimental synchrotron X-ray diffraction data (blue) and the best fit obtained from dynamical X-ray diffraction simulation (red) for (a) 60 nm and (b) 10 nm LSMO layers on STO(001) substrates. In order to obtain the best fit, the LSMO layer was divided into three parts: interface layer with thickness  $t_i$ , intermediate layer with thickness  $t_m$ , and rest of the layer. Different parts of the LSMO layer exhibit dissimilar *c*-axis lattice parameters.

films are shown in Figure 1 and the fitting results for all measured films are listed in Table I.

As can be seen in Figure 1, thin LSMO films exhibit high structural quality throughout the whole crystalline film matrix which is signified by the presence of thickness fringes. Initially, a uniform LSMO film was assumed and dynamical x-ray diffraction calculations were performed using single *c*-axis value of the pseudocubic unit cell over the whole film thickness. Although we were able to match the measured and calculated STO(002) and LSMO(002) Bragg peak positions and intensities, the rest of the XRD pattern showed very poor agreement resulting in a profile residual factor,  $R_p$ , of 0.68 indicating that our model of a uniform film with constant out-of-plane lattice parameter is not correct.<sup>25</sup> As one can notice from Figure 1, besides substrate and film peaks and the thickness fringes, the XRD pattern shows additional features, which are particularly visible in 60 nm film. First, thickness fringes on the left side of the LSMO(002) peak are enhanced as compared to those on the right side. Second, the fringe intensity exhibits modulation, which is notably visible on the right side of the LSMO(002) peak for the 60 nm film. Such additional features can be observed in all films clearly indicating subtle variations in the lattice parameter of the LSMO layer along the out-of-plane direction. In order to properly reproduce the measured XRD profiles, the LSMO layer thickness was divided into three structural parts with three different out-of-plane lattice parameters:  $c_i$ ,  $c_m$ , and  $c_l$  representing *c*-axis lattice parameters at the LSMO/STO interface, intermediate, and the rest of the layer away from the interface, respectively. Dynamical x-ray diffraction simulations of 60 nm LSMO film on STO(001) substrate for different LSMO layer

TABLE I. Best fit results of the dynamical X-ray diffraction simulation to the experimental XRD profiles for the LSMO/STO(001) layers.

| LSMO film thickness (nm) | $c_i$ (Å)        | $t_i$ (u.c.) | $c_m$ (Å)        | $t_m$ (u.c.) | $c_l$ (Å)        | $t_l$ (u.c.) | $t_{total}$ (nm) |
|--------------------------|------------------|--------------|------------------|--------------|------------------|--------------|------------------|
| 10                       | $3.939 \pm 0.05$ | 2            | $3.873 \pm 0.03$ | 3            | $3.847 \pm 0.02$ | 20           | 9.64             |
| 20                       | $3.925 \pm 0.05$ | 2            | $3.860 \pm 0.03$ | 4            | $3.846 \pm 0.02$ | 43           | 18.87            |
| 40                       | $3.925 \pm 0.05$ | 2            | $3.850 \pm 0.03$ | 9            | $3.838 \pm 0.02$ | 92.5         | 39.75            |
| 60                       | $3.935 \pm 0.05$ | 2            | $3.860 \pm 0.03$ | 22           | $3.831 \pm 0.02$ | 132          | 59.85            |

scenarios are presented in the supplementary material.<sup>26</sup> Three different  $c$ -axis values were needed to properly describe: (a) main (002) Bragg peak and thickness fringes, (b) modulation of the thickness fringes, and (c) thickness fringe enhancement on the left side of the (002) Bragg peak. Values  $c_i$ ,  $c_m$ , and  $c_l$  contribute independently to the shape of the XRD spectra and therefore are not correlated. The  $c_i$  lattice parameter contributes to the enhancement of fringe amplitude to the left of the (002) Bragg peak, while  $c_m$  gives rise to thickness fringe modulations. The fitting was performed using genetic fitting algorithm and resulted in  $R_p$  value of 0.23 for the 60 nm thick LSMO film. The measured and fitted x-ray diffraction patterns are shown in Figure 1 for the 10 and 60 nm thick LSMO films. The main fit results and schematic picture of the LSMO layer structural evolution are presented in Figure 2 and Table I. All LSMO films, independent of thickness, contain a 2 unit cell thick interface layer with  $c_i \approx 3.94. The thickness of the intermediate layer with a lattice parameter of  $c_m \approx 3.86\text{--}3.87c$ -axis lattice parameter variation of the main layer,  $c_l$ , as a function of total film thickness. It slightly decreases from  $\sim 3.85$  \AA to  $\sim 3.83$  \AA as the film thickness increases from 10 to 60 nm.$

The most striking feature obtained from the fits is the expansion of the LSMO  $c$ -axis lattice parameter within the first two unit cells of the LSMO/STO interface. The

pseudocubic lattice constant of bulk LSMO material is  $a_p = 3.88, which is smaller than that of the STO substrate ( $a_{STO} = 3.905). Therefore, a reduced  $c$ -axis lattice constant is expected for the film. Away from the interface, such reduction is indeed observed where  $c_m$ ,  $c_l < a_{STO}$ . However, the 2 u.c. interface layer exhibits a lattice constant  $c_i \approx 3.94, which is considerably larger than  $a_{STO}$ . Such behavior cannot be explained by the theory of elasticity where only interatomic bond stretching is involved. Another strain accommodation mechanism, bond bending, is known to play a significant role in perovskite oxides and was already observed experimentally in epitaxial  $\text{Ca}_{1-x}\text{Sr}_x\text{CuO}_2$ ,  $\text{La}_{1-x}\text{Ca}_x\text{MnO}_3$ ,  $\text{LaNiO}_3$ ,  $\text{SrRuO}_3$ , and  $\text{La}_{1-x}\text{Sr}_x\text{MnO}_3$  oxide thin films.<sup>9,10,27,28</sup> The  $B\text{-O}\text{-}B$  bond bending in oxides with the perovskite structure is a direct consequence of a cooperative rotation of corner-connected  $\text{BO}_6$  octahedral units which changes the size and shape of the unit cell.<sup>29,30</sup> Bulk rhombohedral  $\text{La}_{0.67}\text{Sr}_{0.33}\text{MnO}_3$  possesses  $a^-a^-a^-$  octahedral rotational pattern leading to  $R\text{-}3c$  space group with Mn-O-Mn bond angles of  $166^\circ\text{--}167^\circ$  and Mn-O bond lengths of  $1.954<sup>31</sup> LSMO film unit cell under epitaxial tensile stress exhibits  $a^+a^-c^0$   $\text{MnO}_6$  rotational pattern resulting in a monoclinic unit cell with  $Cmcm$  space group where the absence of octahedral rotations along [001] out-of-plane direction leads to the increase of the in-plane lattice parameter.<sup>10</sup> This tensile strain accommodation takes place in the intermediate and main layers of the LSMO film grown on STO(001) substrates. However, the interface layer exhibits an unusual  $c$ -axis expansion which cannot be explained by the described octahedral tilts and rotations.$$$$

We now focus on the mechanism of  $c$ -axis lattice expansion within the first two unit cells of the LSMO film. Figure 3 shows the relationship between the out-of-plane lattice parameter of a strained pseudocubic  $\text{La}_{1-x}\text{Sr}_x\text{MnO}_3$  as a function of Sr content assuming three different octahedral rotational patterns:  $a^-a^-a^-$  as for bulk LSMO (blue rhombuses),  $a^+a^-c^0$  as for tetragonal LSMO films under tensile stress (green triangles), and  $a^0a^0a^0$  as for cubic LSMO structure with straight Mn-O-Mn bonds (red squares). The Mn-O bond lengths,  $d_{\text{Mn-O}}$ , were obtained from  $\sim 30$  powder diffraction files of bulk  $\text{La}_{1-x}\text{Sr}_x\text{MnO}_3$  data listed in the PDF-4+ database of the International Centre for Diffraction Data. The strained out-of-plane lattice parameter  $c_L$  was calculated using the following equation:

$$C_L = -\frac{2\nu}{1-\nu} (a_{STO} - a_L^R) + a_L^R, \quad (1)$$

where the relaxed pseudocubic lattice parameter  $a_L^R$  was estimated from rhombohedral, tetragonal, and cubic LSMO unit cells, the substrate lattice parameter  $a_{STO} = 3.905 and$

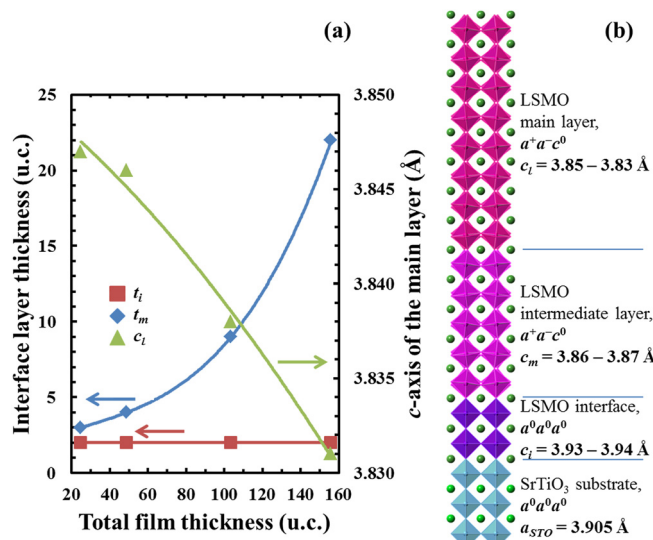


FIG. 2. Structural evolution of the LSMO thin film along the out-of-plane direction: (a) variation of the interface and intermediate layer thickness and  $c$ -axis lattice parameter of the main layer as a function of total film thickness, (b) schematic diagram of the LSMO layer structural evolution near and away from the LSMO/STO interface.

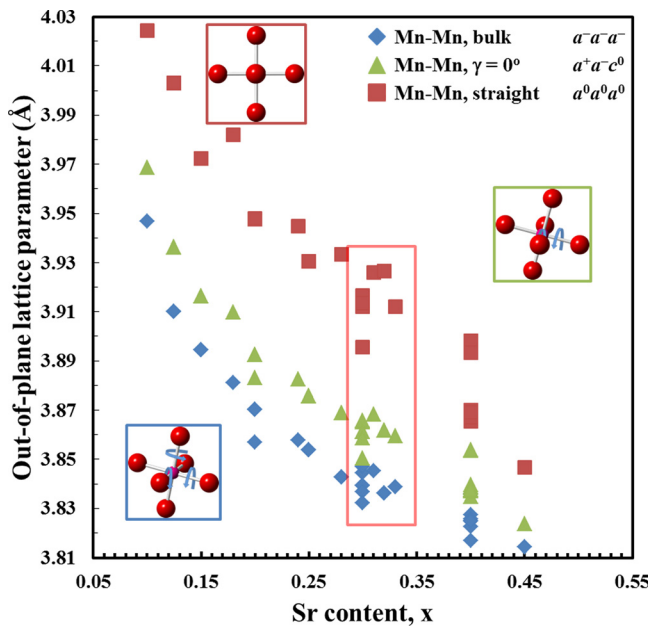


FIG. 3. Change of the out-of-plane lattice parameter as a function of Sr content for different  $\text{MnO}_6$  octahedral tilt scenarios: red squares—straight octahedra, no tilt, green triangles—octahedral tilts about in-plane  $a$  and  $b$  axes only, blue rhombuses—out-of-phase octahedral tilts about  $a$ ,  $b$ , and  $c$  axes as in bulk  $\text{La}_{1-x}\text{Sr}_x\text{MnO}_3$ .

the Poisson ratio  $\nu = 0.4$ . Here, we used a Poisson ratio of 0.4 deduced from the measurements of  $\text{La}_{0.83}\text{Sr}_{0.17}\text{MnO}_3$  single crystal at 300 K by Darling *et al.*<sup>32</sup> This value is valid for rhombohedral LSMO with  $x = 0.17$ . Slightly lower Poisson values of  $\nu = 0.33$ – $0.34$  were reported for twinned LSMO/STO(001) films with  $x = 0.33$ , which would change our estimated out-of-plane lattice parameter by  $<0.2\%$ .<sup>33,34</sup>

The highlighted region in Figure 3 represents data for Sr content  $x = 0.29$ – $0.35$ , which clearly indicates that only straight Mn-O-Mn bonds can explain the expanded LSMO  $c$ -axis lattice parameter at the interface. We can conclude that at the LSMO/STO interface the film exhibits  $a^0a^0a^0$  octahedral rotational pattern, i.e., no rotations are present within first 2 unit cells. The  $c$ -axis lattice parameter of the intermediate layer,  $c_m$ , is in perfect agreement with data shown in Figure 3 (green triangles) for  $x \approx 0.3$  confirming  $a^+a^-c^0$  rotational pattern in this region. The rest of the layer possesses similar rotational pattern as the intermediate layer but evolves further by slightly reducing out-of-plane lattice parameter from  $\sim 3.86 \text{ \AA}$  to  $\sim 3.83$ – $3.85 \text{ \AA}$  which depends on the total film thickness. The suppression of octahedral rotations at LSMO/STO interface layer is a direct consequence of the symmetry mismatch between LSMO and STO crystallographic structures and inherent interfacial octahedral coupling across the LSMO/STO interface.<sup>13,14,35</sup> The STO unit cell symmetry is  $Pm-3m$  and belongs to a zero tilt system  $a^0a^0a^0$  while thick LSMO layer under tensile strain possesses  $Cmcm$  symmetry and exhibits  $a^+a^-c^0$  rotational pattern. In order to maintain corner connectivity between  $\text{TiO}_6$  and  $\text{MnO}_6$  octahedral units across the substrate-film interface, the film's unit cell is forced to adapt symmetry of the STO substrate by straightening Mn-O-Mn bonds and acquiring  $a^0a^0a^0$  tilt system. Consequently, the LSMO out-of-plane lattice constant at the interface should become  $c_i = 2 \times d_{\text{Mn-O}}$ ,

depending on the actual Mn-O bond length,  $d_{\text{Mn-O}}$ , which for  $x = 0.29$ – $0.35$  varies from  $1.954$  to  $1.959 \text{ \AA}$ . Within this La/Sr ratio, the straight Mn-O-Mn bond length is larger than the lattice constant of STO substrate and thus Mn-O bond is compressed in-plane and, depending on a Poisson ratio of the LSMO material, film's  $c$ -axis lattice parameter increases beyond Mn-O-Mn bond length as shown in Figure 3.

The  $a^0a^0a^0$  tilt system and consequent in-plane bond compression while the out-of-plane Mn-O-Mn bond is elongated modifies orbital ordering of a Mn atom. The described deformation of  $\text{MnO}_6$  octahedra is related to  $Q_3$  J-T distortion which lifts the degeneracy of  $e_g$  orbitals by placing  $(3z^2 - r^2)$  state lower in energy as compared to  $(x^2 - y^2)$  state. As a result the  $(3z^2 - r^2)$  orbitals are expected to be preferentially occupied by an electron and leaving  $(x^2 - y^2)$  orbitals empty. Indeed, the orbital symmetry breaking effects at the LSMO/STO interface were reported by Tebano *et al.* using linear dichroism of the x-ray absorption (LD-XAS) at 10 K where evidence of preferential  $(3z^2 - r^2)$  occupation was observed in 6 u.c. thick films.<sup>7</sup> It is important to point out that the J-T distortion induced by the suppression of octahedral rotations is rather small, in the order of  $0.01$ – $0.03 \text{ \AA}$  and therefore is very sensitive to Mn-O bond length variation with temperature, which might explain contradictory LD\_XAS results obtained at 100 K by Huijben *et al.*<sup>23</sup> The J-T distortion is probably connected to the dead-layer in electrical transport in ultrathin LSMO films. The elongation of the  $c$ -axis parameter within first 3 LSMO u.c. in LSMO/STO(001) thin films was also observed by Herger *et al.* using surface x-ray diffraction technique.<sup>6</sup> While the reported results perfectly agree with our observations, the effect was attributed to Sr segregation at the film surface. We would like to rule out the influence of Sr composition variation on the  $c$ -axis lattice parameter at the LSMO interface layer in our samples. As can be seen from Fig. 3, in order to achieve out-of-plane lattice parameter of  $\sim 3.94 \text{ \AA}$  in bulk LSMO, Sr composition has to reach values of  $x \approx 0.1$ – $0.13$  which results in  $\sim 70\%$  loss of Sr in the LSMO interface layer. Such drastic reduction of Sr in only 2 u.c. of LSMO layer seems highly unlikely. Another cause of LSMO lattice expansion is the oxygen loss at the interface. For the reported growth conditions, the oxygen stoichiometry at the interface was previously verified by monitoring Mn valence state which is known to be very sensitive to the oxygen content.<sup>36</sup> No difference from bulk Mn valence was observed, confirming uniform oxygen stoichiometry throughout the whole film. Furthermore, in order to check for the possibility of a growth-induced oxygen deficient layer at the film/substrate interface, we grew a sample of slightly oxygen deficient  $\text{SrTiO}_{3-\delta}$  layer on STO(001) substrate. In this case, due to cubic  $Pm-3m$  symmetry of the  $\text{SrTiO}_3$  perovskite structure, octahedral rotations are absent. The fit between high-resolution x-ray diffraction spectra around STO(002) Bragg peak and theoretical dynamical x-ray diffraction simulations revealed that STO layer exhibits constant  $c$ -axis lattice parameter starting from the  $\text{SrTiO}_{3-\delta}/\text{SrTiO}_3$  interface without any indication of  $c$ -axis expansion/contraction near the interface region signifying uniform oxygen distribution.<sup>26</sup>

In summary, we have demonstrated that LSMO/STO(001) thin films undergo complex strain accommodation route along the out-of-plane direction. At the interface,

within first 2 unit cells, film's unit cell assumes symmetry of a cubic STO substrate which leads to the suppressed octahedral rotations and elongated *c*-axis lattice parameter. Farther from the interface, MnO<sub>6</sub> octahedral rotations evolve and assume rotational pattern that is the same as in thicker coherently strained LSMO films. The intermediate region right after interface shows *c*-axis lattice parameter  $c_m < a_{STO}$ , but slightly larger than the rest of the layer which perfectly agrees with  $a^+ a^- c^0$  rotational pattern. The thickness of an intermediate layer changes with total film thickness. The rest of the layer shows the same rotational pattern but with slightly reduced *c*-axis lattice parameter. The results reveal two distinct strain coupling mechanisms: octahedral rotations/deformations due to symmetry mismatch at the interface and octahedral rotations due to lattice mismatch in the rest of the film and offer new routes for strain engineering in functional complex oxide heterostructures.

Use of the Stanford Synchrotron Radiation Lightsource, SLAC National Accelerator Laboratory, was supported by the U.S. Department of Energy, Office of Science, Office of Basic Energy Sciences under Contract No. DE-AC02-76SF00515. This research was financially supported by the Dutch Science Foundation and by NanoNed, a nanotechnology program of the Dutch Ministry of Economic Affairs.

- <sup>1</sup>H. Y. Hwang, T. T. M. Palstra, S. W. Cheong, and B. Batlogg, *Phys. Rev. B* **52**(21), 15046–15049 (1995).
- <sup>2</sup>O. Dieguez, K. M. Rabe, and D. Vanderbilt, *Phys. Rev. B* **72**(14), 144101 (2005).
- <sup>3</sup>C. J. Fennie and K. M. Rabe, *Phys. Rev. Lett.* **97**(26), 267602 (2006).
- <sup>4</sup>J. H. Lee, L. Fang, E. Vlahos, X. L. Ke, Y. W. Jung, L. F. Kourkoutis, J. W. Kim, P. J. Ryan, T. Heeg, M. Roeckerath, V. Goian, M. Bernhagen, R. Uecker, P. C. Hammel, K. M. Rabe, S. Kamba, J. Schubert, J. W. Freeland, D. A. Muller, C. J. Fennie, P. Schiffer, V. Gopalan, E. Johnston-Halperin, and D. G. Schlom, *Nature* **466**(7309), U954–U972 (2010).
- <sup>5</sup>A. J. Millis, T. Darling, and A. Migliori, *J. Appl. Phys.* **83**(3), 1588 (1998).
- <sup>6</sup>R. Herger, P. Willmott, C. Schlepütz, M. Björck, S. Pauli, D. Martoccia, B. Patterson, D. Kumah, R. Clarke, Y. Yacoby, and M. Döbeli, *Phys. Rev. B* **77**(8), 085401 (2008).
- <sup>7</sup>A. Tebano, C. Aruta, S. Sanna, P. Medaglia, G. Balestrino, A. Sidorenko, R. De Renzi, G. Ghiringhelli, L. Braicovich, V. Bisogni, and N. Brookes, *Phys. Rev. Lett.* **100**(13), 137401 (2008).
- <sup>8</sup>J. S. Lee, D. A. Arena, P. Yu, C. S. Nelson, R. Fan, C. J. Kinane, S. Langridge, M. D. Rossell, R. Ramesh, and C. C. Kao, *Phys. Rev. Lett.* **105**(25), 257204 (2010).
- <sup>9</sup>S. J. May, J. W. Kim, J. M. Rondinelli, E. Karapetrova, N. A. Spaldin, A. Bhattacharya, and P. J. Ryan, *Phys. Rev. B* **82**(1), 014110 (2010).
- <sup>10</sup>A. Vailionis, H. Boschker, W. Siemons, E. P. Houwman, D. H. A. Blank, G. Rijnders, and G. Koster, *Phys. Rev. B* **83**(6), 064101 (2011).
- <sup>11</sup>A. Vailionis, W. Siemons, and G. Koster, *Appl. Phys. Lett.* **93**(5), 051909 (2008).
- <sup>12</sup>H. Boschker, M. Mathews, P. Brinks, E. Houwman, A. Vailionis, G. Koster, D. H. A. Blank, and G. Rijnders, *J. Magn. Magn. Mater.* **323**(21), 2632–2638 (2011).
- <sup>13</sup>J. He, A. Borisevich, S. V. Kalinin, S. J. Pennycook, and S. T. Pantelides, *Phys. Rev. Lett.* **105**(22), 227203 (2010).
- <sup>14</sup>A. Y. Borisevich, H. J. Chang, M. Huijben, M. P. Oxley, S. Okamoto, M. K. Nirajan, J. D. Burton, E. Y. Tsymbal, Y. H. Chu, P. Yu, R. Ramesh, S. V. Kalinin, and S. J. Pennycook, *Phys. Rev. Lett.* **105**(8), 087204 (2010).
- <sup>15</sup>R. Aso, D. Kan, Y. Shimakawa, and H. Kurata, *Sci. Rep.* **3**, 2214 (2013).
- <sup>16</sup>J. Hwang, J. Son, J. Y. Zhang, A. Janotti, C. G. Van de Walle, and S. Stemmer, *Phys. Rev. B* **87**(6), 060101(R) (2013).
- <sup>17</sup>T. T. Fister, H. Zhou, Z. Luo, S. S. A. Seo, S. O. Hruszkewycz, D. L. Proffit, J. A. Eastman, P. H. Fuoss, P. M. Baldo, H. N. Lee, and D. D. Fong, *APL Mater.* **2**(2), 021102 (2014).
- <sup>18</sup>E. J. Moon, P. V. Balachandran, B. J. Kirby, D. J. Keavney, R. J. Sichel-Tissot, C. M. Schleputz, E. Karapetrova, X. M. Cheng, J. M. Rondinelli, and S. J. May, *Nano Lett.* **14**(5), 2509–2514 (2014).
- <sup>19</sup>H. Boschker, J. Kautz, E. P. Houwman, W. Siemons, D. H. A. Blank, M. Huijben, G. Koster, A. Vailionis, and G. Rijnders, *Phys. Rev. Lett.* **109**(15), 157207 (2012).
- <sup>20</sup>G. Koster, B. L. Kropman, G. J. H. M. Rijnders, D. H. A. Blank, and H. Rogalla, *Appl. Phys. Lett.* **73**(20), 2920–2922 (1998).
- <sup>21</sup>G. J. H. M. Rijnders, G. Koster, D. H. A. Blank, and H. Rogalla, *Appl. Phys. Lett.* **70**(14), 1888–1890 (1997).
- <sup>22</sup>S. Stepanov, "Advances in computational methods for x-ray and neutron optics," *Proc. SPIE* **5536**, 16–26 (2004).
- <sup>23</sup>M. Huijben, L. W. Martin, Y. H. Chu, M. B. Holcomb, P. Yu, G. Rijnders, D. H. A. Blank, and R. Ramesh, *Phys. Rev. B* **78**(9), 094413 (2008).
- <sup>24</sup>H. Boschker, M. Huijben, A. Vailionis, J. Verbeeck, S. van Aert, M. Luysberg, S. Bals, G. van Tendeloo, E. P. Houwman, G. Koster, D. H. A. Blank, and G. Rijnders, *J. Phys. D: Appl. Phys.* **44**(20), 205001 (2011).
- <sup>25</sup>R. A. Young, *The Rietveld Method*, International Union of Crystallography (Oxford University Press, Chester, England, Oxford, New York, 1993).
- <sup>26</sup>See supplementary material at <http://dx.doi.org/10.1063/1.4896969> for dynamical x-ray diffraction simulations of 60 nm LSMO film on STO(001) substrate for different LSMO layer scenarios (Figures S1–S3) and a dynamical x-ray diffraction best fit of slightly deficient SrTiO<sub>3–δ</sub> layer on single crystal SrTiO<sub>3</sub> substrate (Figure S4).
- <sup>27</sup>A. Miniotas, A. Vailionis, E. B. Svedberg, and U. O. Karlsson, *J. Appl. Phys.* **89**(4), 2134–2137 (2001).
- <sup>28</sup>A. Vailionis, A. Brazdeikis, and A. S. Flodstrom, *Phys. Rev. B* **55**(10), R6152–R6155 (1997).
- <sup>29</sup>A. M. Glazer, *Acta Crystallogr. A* **31**(1), 756–762 (1975).
- <sup>30</sup>C. J. Howard and H. T. Stokes, *Acta Crystallogr. B* **54**, 782–789 (1998).
- <sup>31</sup>P. G. Radaelli, G. Iannone, M. Marezio, H. Y. Hwang, S. W. Cheong, J. D. Jorgensen, and D. N. Argyriou, *Phys. Rev. B* **56**(13), 8265–8276 (1997).
- <sup>32</sup>T. W. Darling, A. Migliori, E. G. Moshopoulou, S. A. Trugman, J. J. Neumeier, J. L. Sarrao, A. R. Bishop, and J. D. Thompson, *Phys. Rev. B* **57**(9), 5093–5097 (1998).
- <sup>33</sup>J. L. Maurice, F. Pailloux, A. Barthelemy, O. Durand, D. Imhoff, R. Lyonnet, A. Rocher, and J. P. Contour, *Philos. Mag.* **83**(28), 3201–3224 (2003).
- <sup>34</sup>F. Sandiumenge, J. Santiso, L. Balcells, Z. Konstantinovic, J. Roqueta, A. Pomar, J. P. Espinos, and B. Martinez, *Phys. Rev. Lett.* **110**(10), 107206 (2013).
- <sup>35</sup>J. M. Rondinelli, S. J. May, and J. W. Freeland, *MRS Bull.* **37**(3), 261–270 (2012).
- <sup>36</sup>H. Boschker, J. Verbeeck, R. Egoavil, S. Bals, G. van Tendeloo, M. Huijben, E. P. Houwman, G. Koster, D. H. A. Blank, and G. Rijnders, *Adv. Funct. Mater.* **22**(11), 2235–2240 (2012).